**Annales
Geophysicae**

# Gravity wave penetration into the thermosphere: sensitivity to solar cycle variations and mean winds

**D. C. Fritts and S. L. Vadas**

NorthWest Research Associates, CoRA Division, 3380 Mitchell Lane, Boulder, CO 80301, USA

**Abstract.** We previously considered various aspects of gravity wave penetration and effects at mesospheric and thermospheric altitudes, including propagation, viscous effects on wave structure, characteristics, and damping, local body forcing, responses to solar cycle temperature variations, and filtering by mean winds. Several of these efforts focused on gravity waves arising from deep convection or in situ body forcing accompanying wave dissipation. Here we generalize these results to a broad range of gravity wave phase speeds, spatial scales, and intrinsic frequencies in order to address all of the major gravity wave sources in the lower atmosphere potentially impacting the thermosphere. We show how penetration altitudes depend on gravity wave phase speed, horizontal and vertical wavelengths, and observed frequencies for a range of thermospheric temperatures spanning realistic solar conditions and winds spanning reasonable mean and tidal amplitudes. Our results emphasize that independent of gravity wave source, thermospheric temperature, and filtering conditions, those gravity waves that penetrate to the highest altitudes have increasing vertical wavelengths and decreasing intrinsic frequencies with increasing altitude. The spatial scales at the highest altitudes at which gravity wave perturbations are observed are inevitably horizontal wavelengths of ∼150 to 1000 km and vertical wavelengths of ∼150 to 500 km or more, with the larger horizontal scales only becoming important for the stronger Doppler-shifting conditions. Observed and intrinsic periods are typically ∼10 to 60 min and ∼10 to 30 min, respectively, with the intrinsic periods shorter at the highest altitudes because of preferential penetration of GWs that are up-shifted in frequency by thermospheric winds.

**Keywords.** Ionosphere (Equatorial ionosphere; Ionosphere-atmosphere interactions; Ionospheric irregularities; Plasma waves and instabilities) – Meteorology and atmospheric dynamics (Middle atmosphere dynamics; Thermospheric dynamics; Waves and tides)

## 1 Introduction

There has been evidence of, and interest in, gravity waves (GWs) in the thermosphere and ionosphere (TI) for many years. Signatures of such motions are termed traveling ionospheric disturbances (TIDs), and observations and modeling suggest that they often originate from auroral sources in the high-latitude thermosphere (Georges, 1968; Francis, 1973; Richmond, 1978; Hickey and Cole, 1988; Hocke and Schegel, 1996; Hocke et al., 1996; Oliver et al., 1997; Djuth et al., 1997, 2004). Other motions believed to arise at lower altitudes typically have phase speeds less than 250 m/s (Hocke and Schlegel, 1996; Waldock and Jones, 1986, 1987; Crowley et al., 1987; Ogawa et al., 1987). GW periods were found to vary with altitude, with smaller periods (∼20 to 60 min) more prevalent in the lower thermosphere and longer periods (∼1 h or longer) accounting for the largest fluctuations at greater altitudes (Thome and Rao, 1969; Hearn and Yeh, 1977; Hung et al., 1978; Hung and Kuo, 1978; Hung and Smith, 1978; Livneh et al., 2007). Vertical wavelengths were also found to vary with altitude, ranging from a few or 10s of km in the lower thermosphere to ∼100 to 300 km significantly above (Oliver et al., 1997; Djuth et al., 1997, 2004; Livneh et al., 2007). Typical horizontal wavelengths also vary with altitude, but apparently to a much smaller degree, being most often in the range of ∼130 to 500 km (Thome and Rao, 1969; Hearn and Yeh, 1977; Samson et al., 1990). It was the pioneering work by Hines (1960, 1967), however, that made the first persuasive arguments that such ionospheric fluctuations were manifestations of GWs propagating in the neutral atmosphere.

As the importance of GWs at high altitudes became more apparent, a wide range of additional studies ensued. A number of these addressed GW sources that appeared to account for thermospheric responses. Taylor and Hapgood (1988), Dewan et al. (1998), and Sentman et al. (2003) provided strong evidence for rapid mesospheric responses to deep convection, with observed patterns of concentric rings and apparent GW horizontal scales ranging from a few tens to

several hundred km. Additional evidence for convective and hurricane sources of GWs at higher altitudes was obtained with radars and GPS measurements of winds and temperatures (Bauer, 1958; Röttger, 1977; Hung et al., 1978; Hung and Kuo, 1978; Hung and Smith, 1978; Tsuda et al., 2000; Hocke and Tsuda, 2001; Bishop et al., 2006). Modeling and theoretical studies also suggested that GWs arising from deep convection could penetrate to mesospheric and lower thermospheric (MLT) altitudes and have corresponding TI responses (Alexander et al., 1995; Piani et al., 2000; Lane et al., 2001; Lane and Clark, 2002; Horinouchi et al., 2002; Vadas and Fritts, 2004, 2006, hereafter VF06; Vadas, 2007, hereafter V07). Studies such as these, and correlations of GW source regions with ionospheric effects such as equatorial spread F and plasma bubbles, led to recurring suggestions that GWs may play a role in seeding these dynamics (Anderson et al., 1982; McClure et al., 1998). These possible links from the lower atmosphere into the TI were the motivation for the Spread F Experiment (SpreadFEx) described by Fritts et al. (2008a) in the issue. An overview of current results is also presented by Fritts et al. (2008b).

Additional studies addressed the propagation and structure of GWs penetrating into the MLT. GW amplitude increases accompanying propagation to high altitudes lead to a range of instability dynamics, turbulence, and effects in the MLT where kinematic viscosity and thermal diffusivity are not sufficient to prevent such dynamics (see Fritts and Alexander, 2003; Fritts et al., 2002, 2006). Importantly, the dynamics of wave breaking and local body forcing (due to local GW momentum flux convergence) are themselves a potentially significant source of additional GWs. These "secondary" GWs often occur on larger spatial scales than the GWs accounting for their generation (Vadas and Fritts, 2001, 2002; Vadas et al., 2003). While their initial amplitudes are very small, those secondary GWs having larger spatial scales and higher frequencies are less influenced by viscous dissipation and preferentially penetrate to much higher altitudes (V07).

The tendency for instability decreases sharply as density decreases (and kinematic viscosity increases) into the thermosphere, and dissipation thereafter is due largely to increasing kinematic viscosity and thermal diffusivity with altitude. This accounts for the "turbopause", which exhibits some variability in altitude that likely results from spatial and temporal variability in GW energy fluxes and propagation conditions. Early efforts to account for GW dissipation at higher altitudes accounted only partially for these damping effects (Pitteway and Hines, 1963; Yeh et al., 1975; Hickey and Cole, 1987). A more recent theory accounting for kinematic viscosity and thermal diffusivity and their variations with altitude assuming a localized, but temporally-varying, GW packet was advanced by Vadas and Fritts (2005, hereafter VF05). This has allowed more complete assessments of GW structure, thermospheric penetration, and momentum transport accompanying increasing dissipation for a wide range of GW scales and propagation conditions (VF06; V07). Indeed,

V07 recently provided an extensive assessment of horizontal and vertical propagation and dissipation for both lower atmospheric and MLT GW sources for a range of GW parameters and for the spectrum of GWs arising from a deep convective plume. Here, we take a different approach and evaluate the fraction of initial GW momentum flux that survives to various altitudes as a function of GW horizontal and vertical wavelength, horizontal phase speed, and observed frequency for a broad range of the spatial and temporal scales expected to impact the TI from both lower atmospheric and MLT GW sources.

We briefly review the anelastic viscous dispersion relation, the assumptions that allow its simple application, and our assumed thermospheric temperature and wind profiles in Sect. 2. Surviving momentum flux fractions as functions of horizontal wavelength for representative initial GW frequencies, thermospheric temperatures, and canonical wind variations are displayed in Sect. 3. Section 4 shows the same results, but as functions of horizontal and vertical wavelength, for the same temperature and wind profiles and observed frequencies. Vertical profiles of momentum flux and normalized body forces as functions of altitude arising for representative GWs for each temperature and wind environment are presented and discussed in Sect. 5. A summary and conclusions are presented in Sect. 6.

## 2 Anelastic viscous dispersion relation and assumptions

We employ the ray tracing methodology described by VF06 to compute GW propagation subject to the full viscous dispersion relation developed by VF05 with a Prandtl number $Pr=\nu/\kappa=0.7$. However, to enhance physical understanding, we display the dispersion relation with the simplifying assumption that $Pr=1$, where $\nu$ and $\kappa$ are kinematic viscosity and thermal diffusivity, respectively, for purposes of computing GW structure, propagation, and dissipation in the MLT. This alters the inferred GW structure and dissipation very little, but greatly simplifies implementation of the viscous dispersion relation. As described by VF05, this approximation alters dissipation altitudes by a fraction of a scale height and a smaller fraction of a typical GW vertical wavelength. The simplified dispersion relation may be written

$$(\omega_{Ir} + \nu m/H)^2 = k_h^2 N^2/(|\boldsymbol{k}|^2 + 1/4H^2), \tag{1}$$

where $\omega_{Ir}=k_h(c-U_h)$ is the real GW intrinsic frequency, $\omega_r=k_h U_h$ is the real GW ground-based frequency, $U_h$ is the component of mean wind in the plane of GW propagation, $k_h$ and $m$ are the GW horizontal and vertical wavenumbers, $k_h=2\pi/\lambda_h$ and $m=2\pi/\lambda_z$, $\lambda_h$ and $\lambda_z$ are the GW horizontal and vertical wavelengths, the total GW wavenumber is $\boldsymbol{k}=(k_h, m)$, $H$ is the density scale height, and $N$ is the buoyancy frequency, assumed to be $N\sim0.02\,\text{s}^{-1}$ (or a period of $\sim5.3\,\text{min}$) at the source level. Where viscosity is negligible,
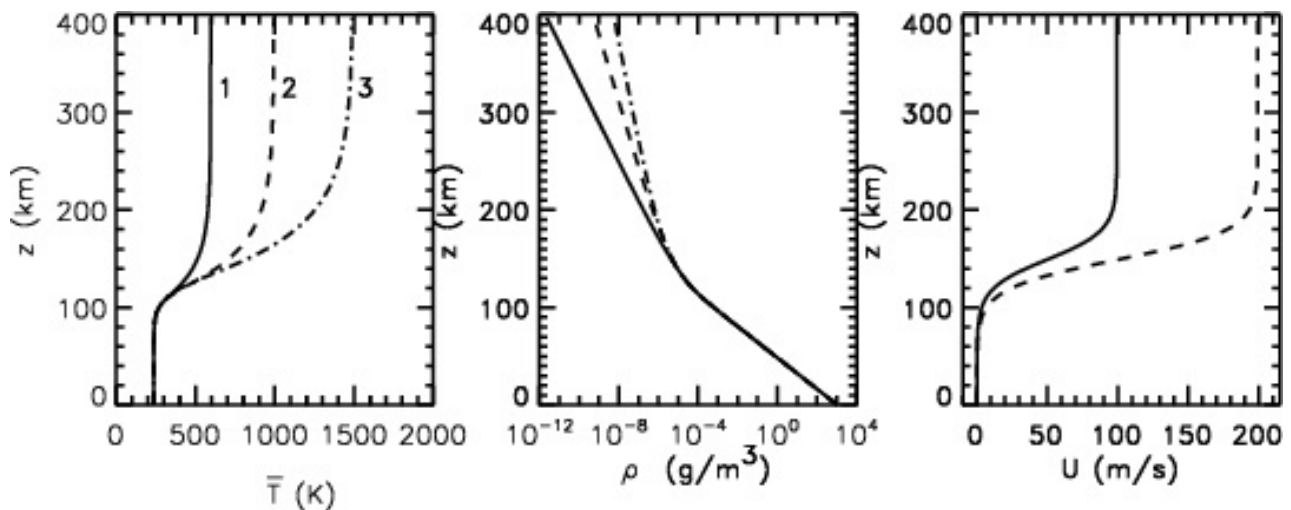
**Fig. 1.** Mean temperatures (left), densities (center), and zonal winds (right) assumed for the computations of GW propagation, dissipation, and momentum flux and divergence discussed in the text. Temperature profiles are assumed to be representative of solar minimum (solid), mean (dashed), and solar maximum (dotted) conditions with asymptotic thermospheric temperatures of 600, 1000, and 1500 K (labeled 1, 2, and 3, respectively). Corresponding densities are shown on a semi-log plot (center). The zonal wind profiles represent nominal and extreme wind speed variations between assumed GW sources in the troposphere and the thermosphere; realistic (primarily tidal) wind variations in the MLT are not included, as only the velocity difference is important for GWs penetrating to high altitudes.

Eq. (1) yields the usual inviscid anelastic dispersion relation of Marks and Eckermann (1995).

Temperature, density, and wind profiles employed for our study are shown in Fig. 1. As the lower atmosphere plays no role in viscous dissipation for the GW scales considered here, we assume it has a uniform temperature of 237 K. Thermospheric temperature profiles are those employed by VF06 and are shown for reference in Fig. 1a. Corresponding mean pressure and density profiles were obtained by integrating the hydrostatic balance equation with $p$, $\rho$, and $T$ related through the ideal gas law (VF06; V07). The mean densities obtained in this manner for each assumed temperature profile are displayed in semi-log plots in Fig. 1b.

To assess filtering and Doppler-shifting effects below, we assume in Sect. 5, we assume a zonal wind that increases from zero to 100 or 200 ms$^{-1}$ over a 60-km depth from 120 to 180 km altitude. The wind profile is given by

$$U(z) = U_0\{1 + \tanh[(z - z_0)/z_1]\}, \tag{2}$$

where $U_0$=50 or 100 ms$^{-1}$ representing moderate and strong Doppler shifting, $z_0$=150 km, and $z_1$=30 km. These profiles are shown in Fig. 1c and are intended to represent the nominal and extreme wind variations expected to be encountered by GWs penetrating to high altitudes without the detailed variations accompanying the variable mean and wave structures in the lower atmosphere or MLT, as these are expected to have no influence below GW dissipation altitudes.

Ray tracing was employed to describe GW vertical propagation, refraction, and viscous dissipation in the wind and temperature fields described above, subject to Eq. (1) and

the WKB and viscous constraints on vertical wavelength described by (V07), both of which require

$$\lambda_z \ll 4\pi H. \tag{3}$$

These conditions place limits on how far we can rely on ray tracing for our purposes in this paper. We will note below where these limits are approached and caution must be exercised.

The interested reader is referred to V07 for a more extensive discussion of these conditions and their implications for GW propagation and ray tracing of GWs penetrating to high altitudes.

## 3 Variations of GW momentum flux with horizontal wavelength

In order to assess the thermospheric penetration of GWs having various initial scales, frequencies, and propagation relative to a zonal mean wind, we have ray traced GWs having initial horizontal and vertical wavelengths of $\lambda_h$=10 to 1500 km and $\lambda_z$=5 to 310 km. Wavelengths outside these ranges are not expected to reach the thermosphere from sources in the lower atmosphere. We also assumed all GWs have an initial momentum flux of unity so as to evaluate relative dissipation of the various GWs with altitude in the variable environments described above. Finally, we have focused on a range of frequencies that we expect to penetrate most efficiently into the thermosphere in the absence of Doppler shifting. The resulting momentum fluxes, $\rho_0 < u'_h w' >$, for ground-based frequencies of $\omega_r$=N/2, N/3,
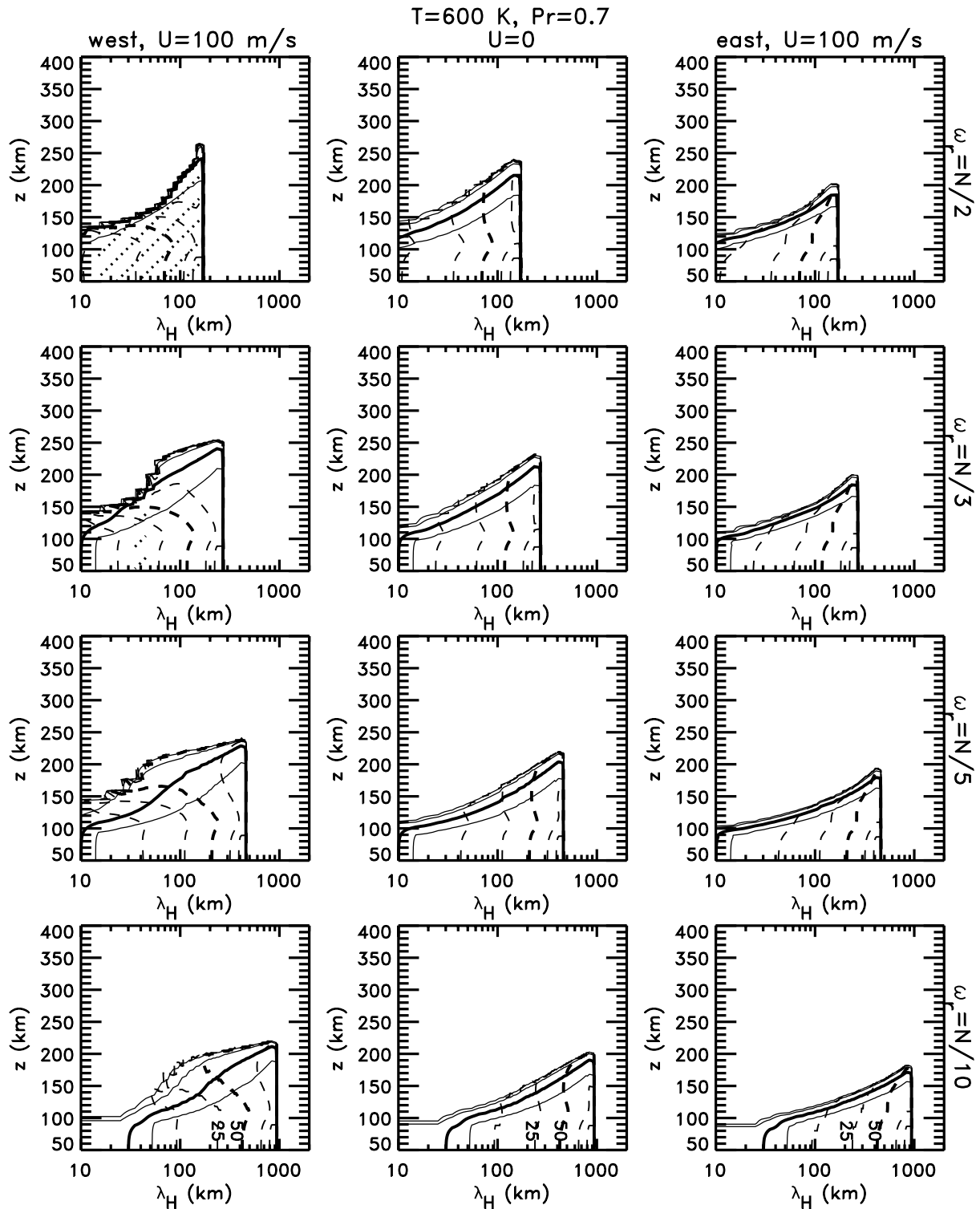
**Fig. 2.** Contour plots of GW momentum flux ($\rho_0(z)<u'_h w'>$) variations with altitude for GWs having horizontal wavelengths varying from 10 to ~1000 km for initial GW frequencies of N/2, N/3, N/5, and N/10 (top to bottom). Left, center, and right panels show results for GWs propagating westward, meridionally (i.e. no wind), and eastward, respectively, in the wind profile shown in Fig. 1c. All GWs were assumed to have unity momentum flux at source levels in the lower atmosphere. Maximum horizontal wavelengths are limited for higher frequencies by the $1/4H^2$ term and the requirement that $m^2$ in Eq. (1) is sufficiently large to satisfy WKB assumptions. Also shown with dashed lines in each panel are contours of vertical wavelength (in km), with 50 km in bold. Momentum flux contour intervals are 0.9, 0.5 (bold), 0.1, and 0.03.
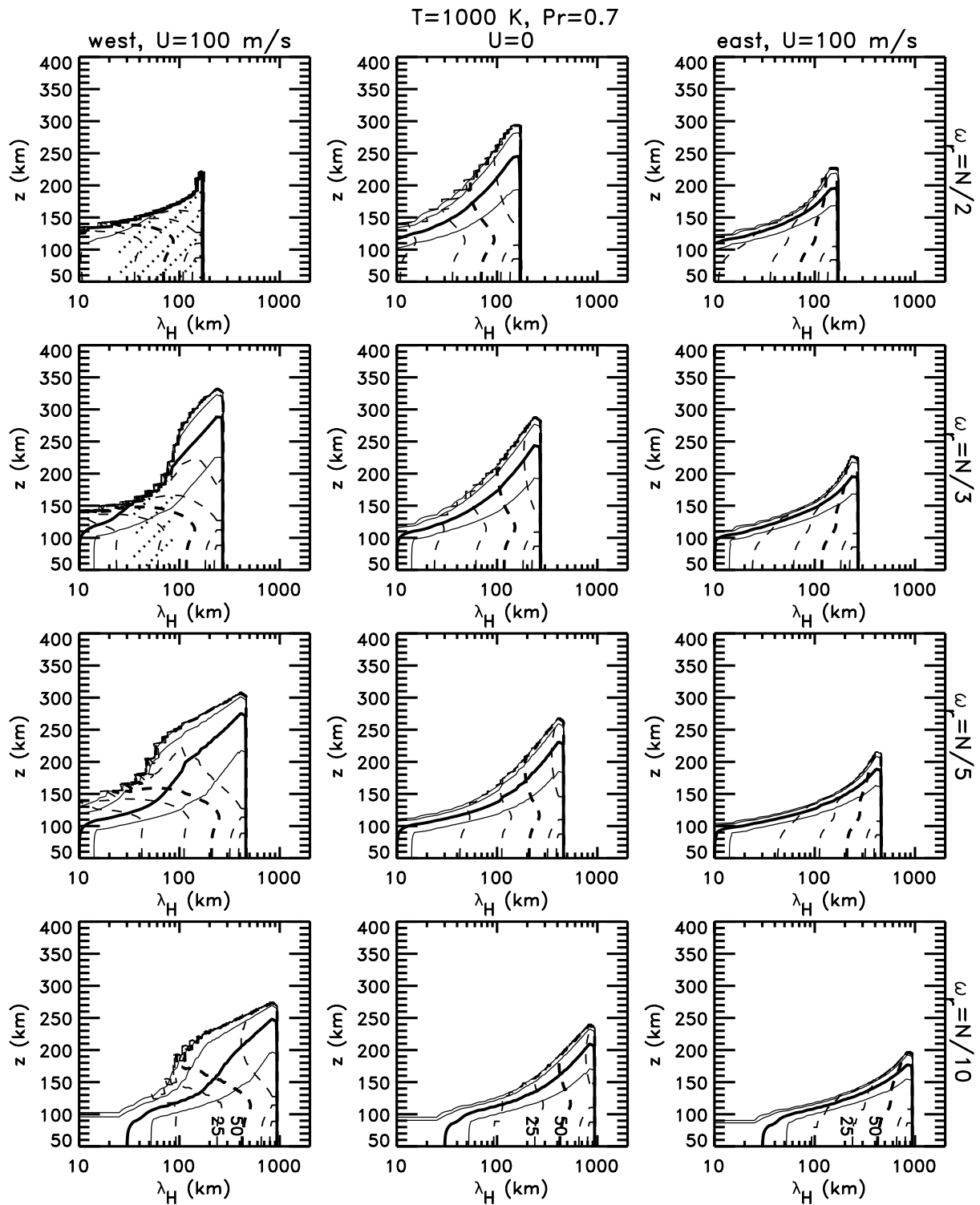
**Fig. 3.** As in Fig. 2, but for mean solar forcing and thermospheric temperatures ($\sim$1000 K).

N/5, and N/10 (corresponding to observed periods of $\sim$10, 15, 30, and 60 min) and a mean wind variation in the lower thermosphere given by Eq. (2) with $U_0$=50 ms$^{-1}$ (a mean wind of 100 ms$^{-1}$) are shown with solid contours at 0.03,

0.1, 0.5 (bold), and 0.9 fractions of the initial momentum flux for the assumed minimum, mean, and maximum solar forcing temperature profiles, respectively, in Figs. 2 to 4. The left, middle, and right panels in each figure are for
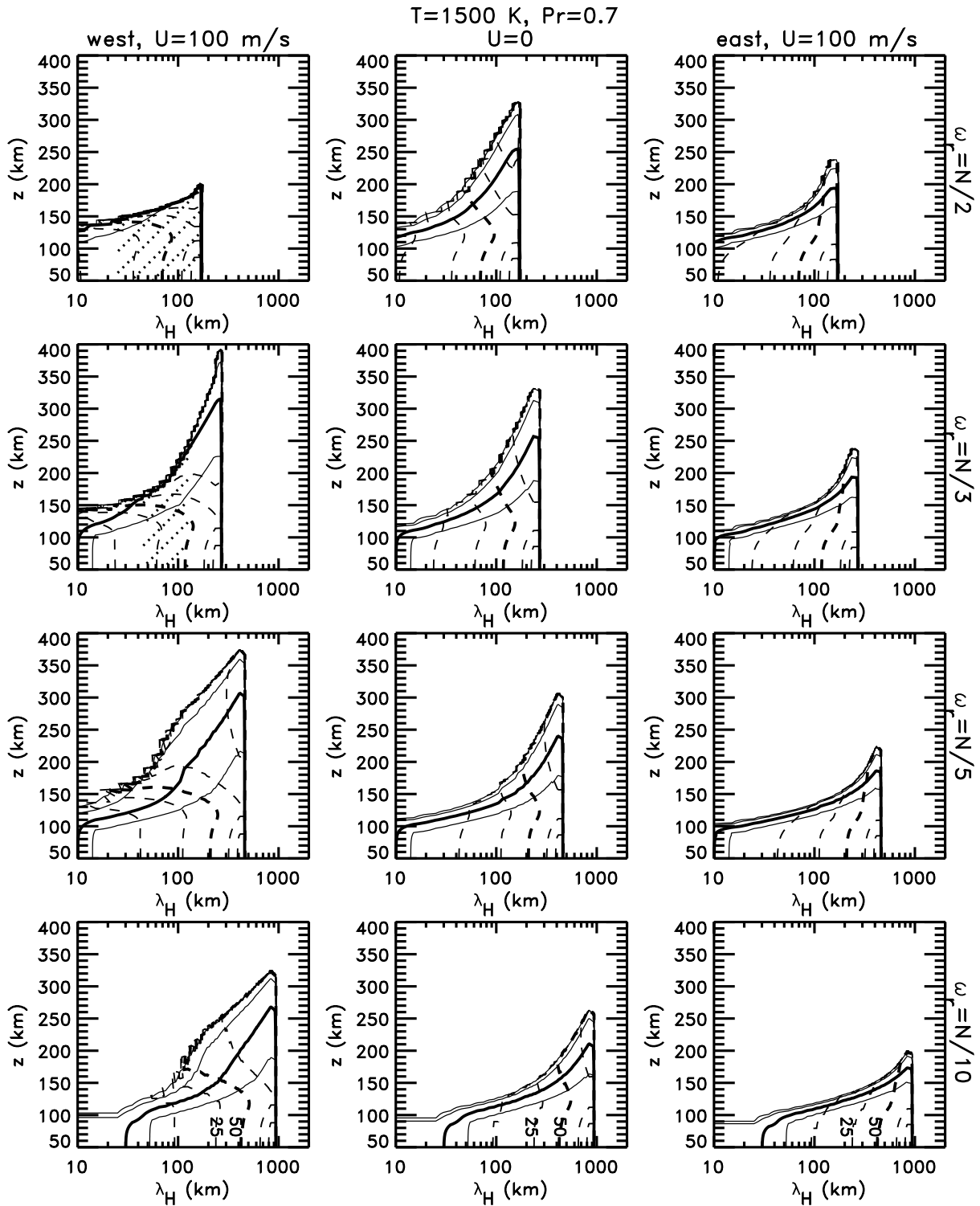
**Fig. 4.** As in Fig. 2, but for maximum solar forcing and thermospheric temperatures (∼1500 K).

GW propagation to the west, meridionally, and to the east (also referred to as up-shifted, unshifted, and down-shifted, respectively), and dashed lines indicate vertical wavelengths in each case, with contour values of 10, 25, 50 (heavy dashed line), 100, and 150 km. Note that the largest $\lambda_h$ are limited for higher frequencies by the $1/4H^2$ term in Eq. (1) because the maximum frequency obtainable for a ground-based GW (that is not dissipating) is $\omega_{\mathrm{Ir}}/N \sim 4\pi H/\lambda_h$. Finally, because

we discretize the GW spectrum in order to use ray tracing to track GW properties and remaining momentum flux, we have smoothed both the momentum flux and vertical wavelength contours in all figures. Nevertheless, the smallest momentum flux contours at the highest altitudes for each horizontal wavelength in Figs. 2 to 4 exhibit some uncertainty because some of these GWs are susceptible to reflection at turning levels, do not propagate to higher altitudes, and are not dissipated strongly (see below).

Considering first the results displayed in Fig. 2, we see that no GWs excited in the lower atmosphere are expected to penetrate above ∼250 km under minimum solar forcing conditions, except for those GWs propagating westward against the assumed mean wind that are Doppler-shifted to higher intrinsic frequencies (up-shifted and refracted to larger $\lambda_z$). Of the up-shifted GWs that do reach higher altitudes, there are ranges of horizontal wavelengths at the higher ground-based frequencies ($\lambda_h$ ∼15 to 150 km for $\omega_r$=N/2 and $\lambda_h$ ∼30 to 50 km for $\omega_r$=N/3) that refract until they reach a turning level, reflect, and fail to propagate to higher altitudes. For all initial frequencies, those GWs achieving the highest altitudes before encountering strong dissipation or a turning level are those that both 1) have the largest (allowed) $\lambda_h$ and 2) are refracted to the largest $\lambda_z$ (highest intrinsic frequencies) at the right edge of each panel. Of these two effects, the first is apparent in the higher $\lambda_z$ associated with the higher $\lambda_h$ at the right edge of each panel arising from the $1/4H^2$ term in Eq. (1). The second effect is only seen in the refraction to larger $\lambda_z$ with increasing altitude (a Doppler shifting to higher intrinsic frequencies) for those GWs propagating against the mean wind. Indeed, it is the GWs that are only just allowed to propagate vertically at lower altitudes (with the largest $\lambda_h$ and minimum positive $m^2$ in Eq. 1) that attain the highest altitudes, independent of all other parameters and propagation directions.

Figures 3 and 4 display the same results shown in Fig. 2 and discussed above, but for the assumed mean and maximum solar forcing temperature profiles. In all cases, the variations with $\lambda_h$, initial frequency, and propagation direction have the same tendencies as in Fig. 2. The interesting aspects are the differences in GW penetration among the different temperature profiles and propagation directions. Higher thermospheric temperatures elevate thermospheric densities, thus decreasing kinematic viscosity and thermal diffusivity (and GW damping) at any given altitude. This increases penetration into the thermosphere for all GWs that continue to propagate vertically, and favors those GWs with higher (up-shifted rather than down-shifted) frequencies. This tendency is seen clearly for $\omega_r$=N/3, N/5, and N/10 in Figs. 3 and 4. However, increasing thermospheric temperatures also decrease N, causing GWs having higher intrinsic frequencies at higher altitudes to be susceptible to reflection at turning levels, which prevent them from influencing plasma dynamics at significantly higher altitudes. As discussed above for minimum solar forcing, this is most apparent for the up-shifted

GWs with $\omega_r$=N/2 (upper left panels in Figs. 3 and 4). The two effects together lead to preferential penetration to higher altitudes of GWs having the largest $\lambda_h$ and experiencing up-shifting of intrinsic frequencies, except at the highest initial frequencies. GWs propagating meridionally (and unshifted in initial frequency) likewise benefit from reduced thermospheric stability and viscosity, but without encountering turning levels. Except at the largest $\lambda_h$ and initial frequency, however, unshifted GWs still fail to penetrate as high as the up-shifted GWs. Down-shifted GWs, in contrast, experience only modest increases in penetration altitudes at higher thermospheric temperatures, with the most significant increases of ∼50 km at the largest $\lambda_h$ and the larger initial frequencies. In particular, the left panels of each figure indicate that GWs having the largest allowed $\lambda_h$ at intermediate initial frequencies (N/3 and N/5) experience the greatest altitude increases, with 10 to 50% of the momentum flux surviving an additional ∼100 km or more. Smaller surviving momentum flux fractions extend as high as ∼350 to 400 km altitudes. Indeed, it is these GWs, that are Doppler shifted from lower initial to higher intrinsic frequencies, but which also avoid reflections at turning levels due to varying winds and temperatures, that must dominate the responses at the highest altitudes, if the primary GW sources are in the lower atmosphere. Despite their likely very small initial amplitudes and their small surviving momentum fluxes, the ∼10 decades of density decrease between GW source levels and the highest altitudes to which these GWs penetrate suggest that they may nevertheless achieve significant amplitudes and neutral and/or plasma responses in the TI system. These possible responses will be explored more fully in Sect. 5 below.

The tendency for reflection of up-shifted GWs at the higher frequencies noted above has major implications for penetration of GWs, or lack of, into the thermosphere. The occurrence of reflection is indicated in Figs. 2 to 4 by slanted dotted lines spanning the relevant range of $\lambda_h$ in each panel. These effects span the majority of the $\lambda_h$ distribution for all thermospheric temperatures for $\omega_r$=N/2 ($\lambda_h$ ∼20 to 200 km), but only limited ranges of $\lambda_h$ at $\omega_r$=N/3 ($\lambda_h$ ∼30 to 70 km and ∼60 to 120 km, respectively, for mean and maximum solar forcing), with no reflection occurring for the two lower initial frequencies considered. In cases where reflections are anticipated, we must also be cautious in estimating surviving momentum flux fractions, as this becomes a challenging process (because momentum fluxes that are estimated to be large at lower altitudes may be suddenly removed from the spectrum due to reflection at a turning level). As a result, the contours of surviving momentum flux where reflections occur are likely artificially somewhat elevated in altitude. This impacts primarily the upper edges of the affected distributions (top left panel in Fig. 2 and upper two left panels in Figs. 3 and 4), but it does not impact the discussion of the GWs penetrating to the highest altitudes above.

Intrinsic periods of the GWs penetrating to the highest altitudes may be inferred from Eq. (1) and the contours of $\lambda_z$
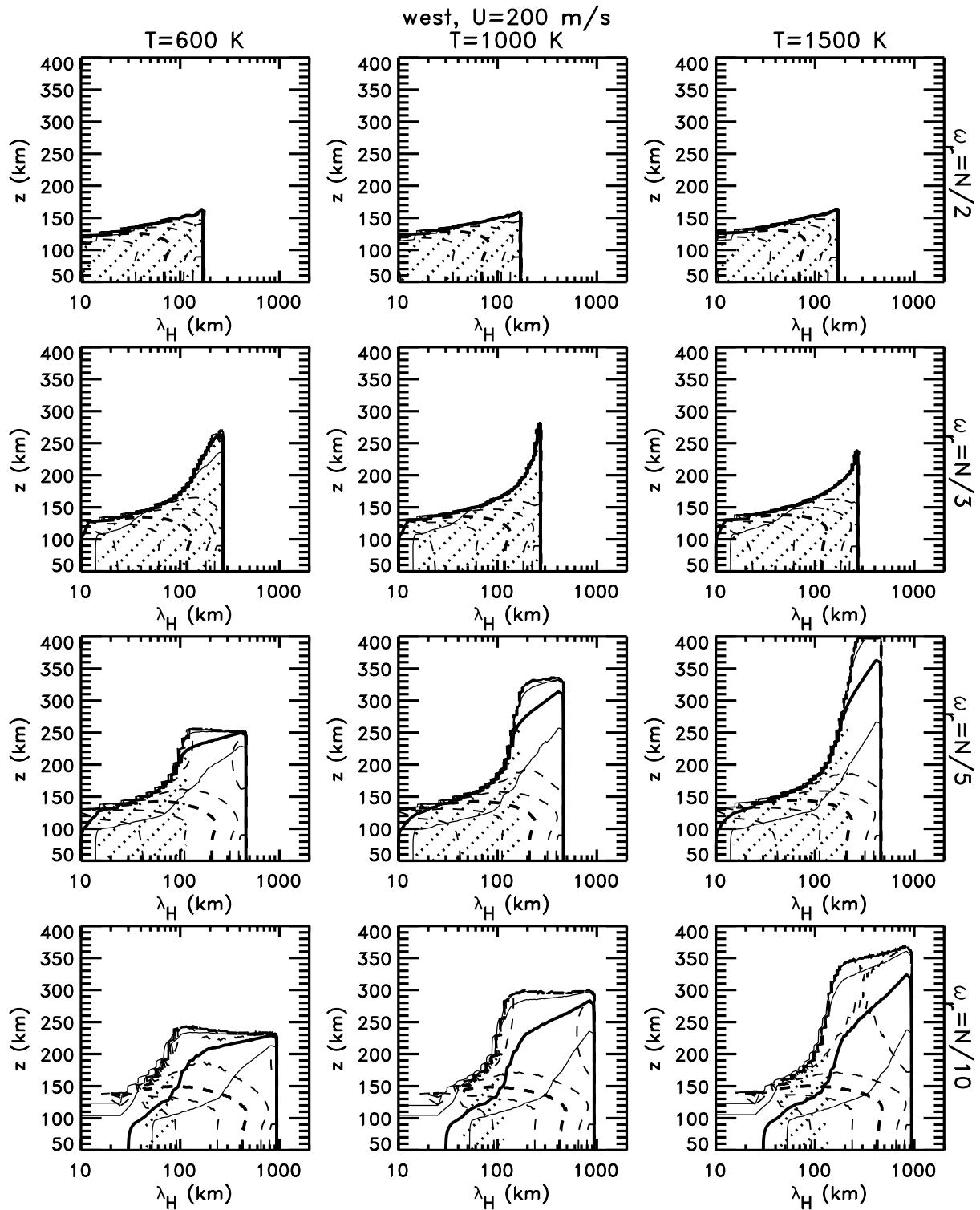
**Fig. 5.** As in Figs. 2 to 4, but for westward-propagating (up-shifted) GWs for minimum, mean, and maximum solar forcing (left, middle, and right columns, respectively) with an eastward thermospheric wind of $200\,\mathrm{ms}^{-1}$.

displayed in Figs. 2 to 4. For the GWs penetrating most effectively to higher altitudes, these are typically within a factor of 2 or 3 of the local buoyancy period (~10 to 30 min). For GWs having larger initial periods or experiencing no Doppler shifting or a down-shifting of intrinsic frequencies due to mean winds (an increase in intrinsic periods), implied periods vary from ~5 to 50 times the loca buoyancy period (intrinsic periods of ~1 to 10 h) and these GWs do not escape the lower thermosphere. Additional discussion of GW periods in the thermosphere accompanies our evaluation of surviving GW momentum flux fractions as functions of $\lambda_h$ and $\lambda_z$ below.

We now consider the effects of stronger Doppler shifting (up-shifting) of those GWs propagating against the eastward mean flow, as we found in the discussion above that up-shifted GWs preferentially penetrate to the highest altitudes. The results of up-shifting with a zonal wind given by Eq. (2) with $U_0$=100 ms$^{-1}$ (a mean wind of 200 ms$^{-1}$) for the three solar forcing conditions are show together in Fig. 5. Comparing these results with those shown in Figs. 2 to 4, we see that there are several major differences. First, the exclusion from propagation to very high altitudes by turning levels impacts a much larger fraction of GWs having high initial frequencies than for the smaller mean wind. Indeed, turning levels now cause the reflection of virtually all of the GWs having an initial ground-based frequency of $\omega_r$=N/2 and much larger fractions of those at lower frequencies, $\omega_r$=N/3 and N/5. The highest penetration occurs for greater Doppler shifting only at the largest horizontal wavelengths, and only marginally higher altitudes are achieved for all solar conditions. Penetration altitudes increase for greater Doppler shifting, with altitude increases ranging from ~20 km at minimum solar conditions to ~50 km at maximum solar conditions. For all cases, however, the fraction of horizontal wavelengths that escapes reflection shrinks, with only $\lambda_h$~100 to 200 km and longer penetrating to the highest altitudes for $\omega_r$=N/5 and N/10, with the larger threshold appropriate for maximum solar forcing conditions. The highest penetration altitudes still occur under maximum solar forcing conditions; however, they shift from $\lambda_h$~150 to 400 km at $\omega_r$=N/2 for Doppler shifting of 100 ms$^{-1}$ to $\lambda_h$~200 to 600 km at $\omega_r$=N/3 for Doppler shifting of 200 ms$^{-1}$, with penetration for GWs with $\lambda_h$ up to ~1000 km to altitudes only ~1 scale height lower. Corresponding down-shifted GWs for stronger Doppler shifting conditions typically penetrate from ~20 to 50 km lower than for weaker Doppler shifting conditions, with the largest differences occurring for the highest initial frequencies and the strongest solar forcing. This occurs because those GWs that avoid critical levels and penetrate through the wind shear are refracted to substantially smaller intrinsic phase speeds having smaller vertical wavelengths that result in dissipation at lower altitudes.

## 4 Variations of GW momentum flux with horizontal and vertical wavelength

We now display the results of our ray tracing in a different form that illustrates the evolutions of GW spatial structures, preferred $\lambda_h$ and $\lambda_z$, and intrinsic wave periods more directly. Shown with solid lines in Figs. 6 to 8 are contours of GW momentum flux as functions of $\lambda_h$ and $\lambda_z$ for the same propagation directions, thermospheric temperatures, and zonal mean wind assumed for Figs. 2 to 4, but now at specific altitudes (150, 200, 225, and 250 km for minimum solar forcing in Fig. 6 and 150, 200, 250, and 300 km for mean and maximum solar forcing in Figs. 7 and 8). Momentum flux contours are again shown at 0.9, 0.5 (bold), 0.1, and 0.03 of the initial value in each case. Also shown in each panel to aid our discussion are contours of observed (ground-based) periods, with dashed lines at 10, 20 (bold dashed line), 30, and 60 min.

We again first consider the results for minimum solar forcing and thermospheric temperatures displayed in Fig. 6. These plots reveal bands extending from $\lambda_h$~50 to 1000 km and $\lambda_z$~20 to 200 km in which ~50 to 90% of the initial momentum flux survives to 150 km, though the vertical wavelengths differ from initial values due to refraction of the eastward- and westward-propagating GWs by zonal mean winds, and of all GWs by the varying temperature profiles with altitude. Note, in particular, the agreement of these inferences with the results displayed in Fig. 2, including the inferences of higher $\lambda_z$ and intrinsic frequencies at the same $\lambda_h$ for westward-propagating than for eastward-propagating GWs. As we might infer from Fig. 2, the disparities between different propagation directions increase with altitude (and zonal mean wind). Eastward-propagating (down-shifted) GWs are largely dissipated by 200 km, but there is still a range of wavelengths for westward-propagating (up-shifted) GWs ($\lambda_h$~100 to 1000 km and $\lambda_z$~100 to 250 km) having surviving momentum flux fractions of ~0.5 to 0.9. At 225 km, unshifted GWs have largely disappeared, except for a small region of 0.1 surviving momentum flux fraction at $\lambda_h$ and $\lambda_z$ ~100 km. Up-shifted GWs are also further restricted, with a surviving fraction of 0.5 at $\lambda_h$~150 to 400 km and $\lambda_z$~100 to 200 km. Surviving momentum fluxes at 250 km are even smaller, ~0.1 or less, and further restricted to $\lambda_h$ and $\lambda_z$~100 to 200 km. The majority of these vertical wavelengths are sufficiently below the value of $4\pi H$ (shown with horizontal dashed lines in each panel), near which the WKB approximation fails, that these plots are likely fairly quantitative in their characterization of GW scales. Nevertheless, we should regard the results for the up-shifted GWs having the largest vertical scales to be approximations to their true structure, amplitudes, and momentum fluxes where Eq. (3) is not strictly satisfied.

Considering the effects of stronger solar forcing, we see from Figs. 7 and 8 that increasing thermospheric temperatures increase the fraction of GWs having appreciable
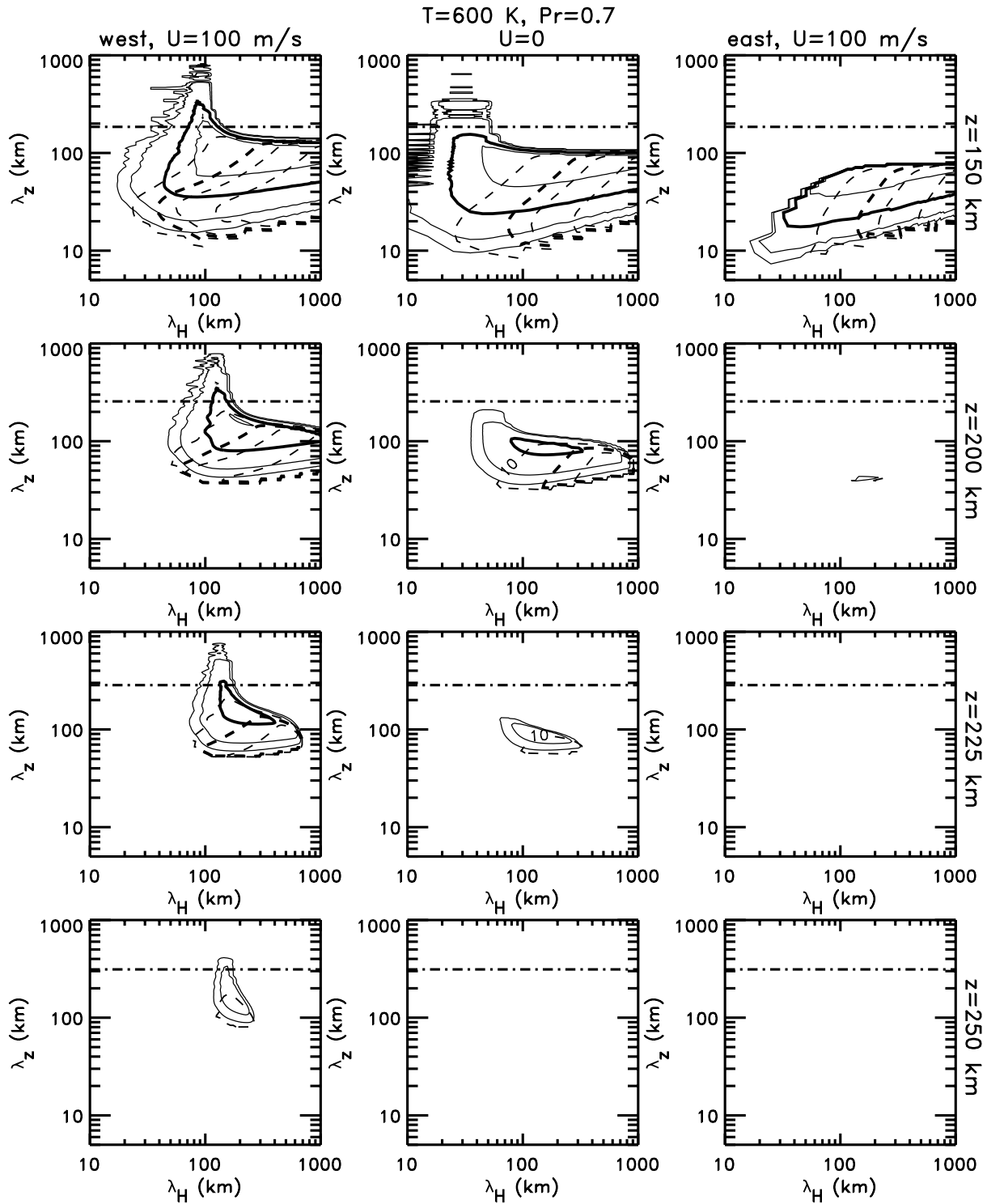
**Fig. 6.** Contour plots of momentum flux magnitudes as functions of horizontal and vertical wavelength at minimum solar forcing ($\sim$600 K thermospheric temperature) for GWs propagating westward, meridionally (i.e. no wind), and eastward (left, center, and right panels, respectively) for the wind profile shown with a solid line in Fig. 1c. Successive plots are at altitudes of 150, 200, 225, and 250 km (top to bottom, respectively). Contour intervals are 0.9, 0.5 (bold), 0.1, and 0.03, and dashed contours indicate observed GW periods of 10, 20 (bold), 30, and 60 min. Vertical wavelengths are not reliable near the value of $4\pi H$ (shown with the horizontal dashed line in each panel) because the WKB assumption is violated at these scales.
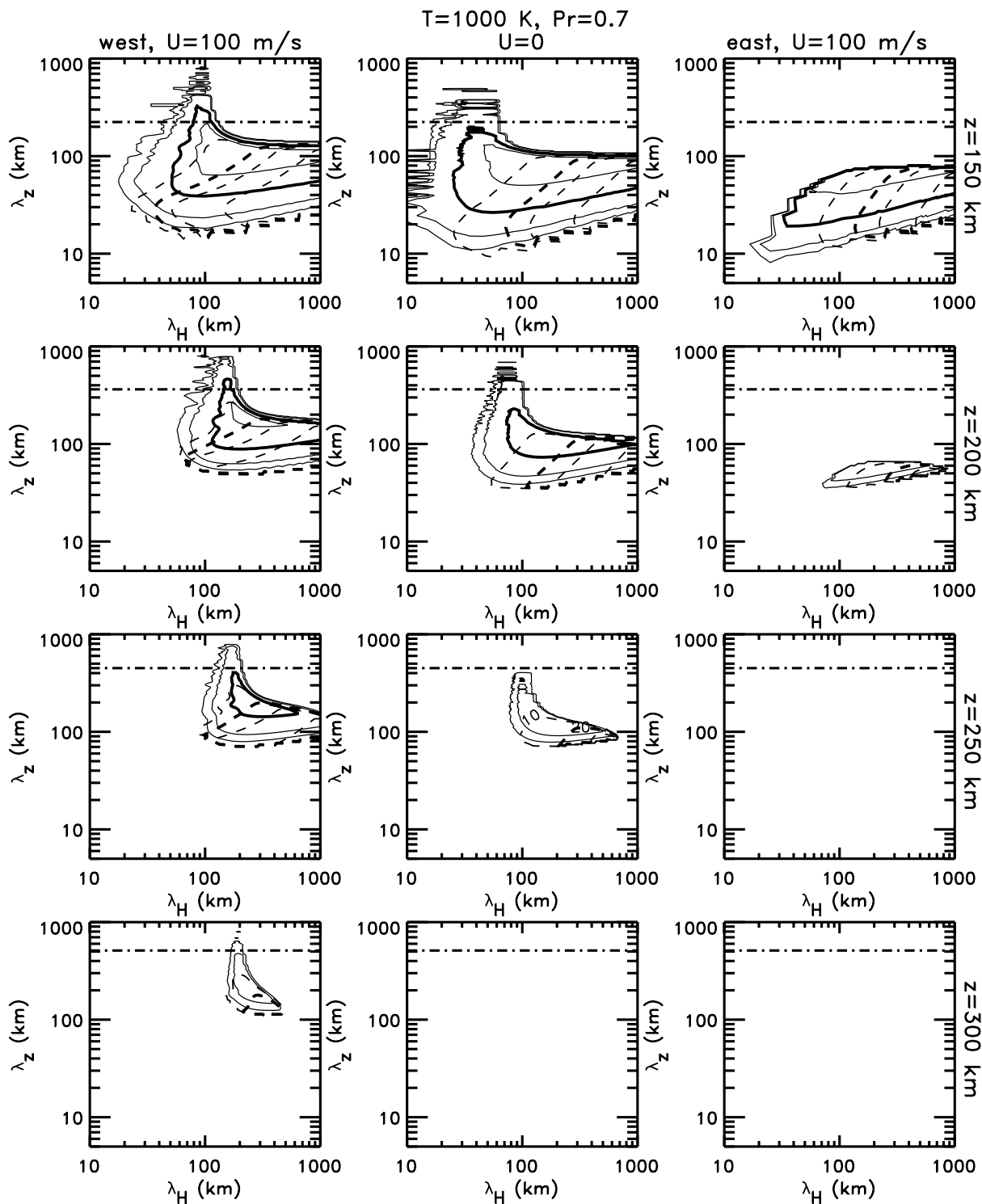
**Fig. 7.** As in Fig. 6, but for mean solar forcing conditions ($\sim$1000 K thermospheric temperature). Note that the vertical wavelength of $4\pi H$ (shown with the horizontal dashed line in each panel), near which WKB theory does not apply, increases with solar forcing.

penetration into the thermosphere for all directions of GW propagation at 200 km and above. For westward-propagating GWs, it also shifts the ranges of $\lambda_h$ and $\lambda_z$ having the highest surviving momentum flux fractions to slightly larger

values. Changes in the westward-propagating GW field at 200 km suggest shifts of the dominant $\lambda_h$ and $\lambda_z$ of $\sim$50 to 100%, with even greater shifts occurring at 250 km. Importantly, both the surviving momentum flux fractions, $\sim$0.03
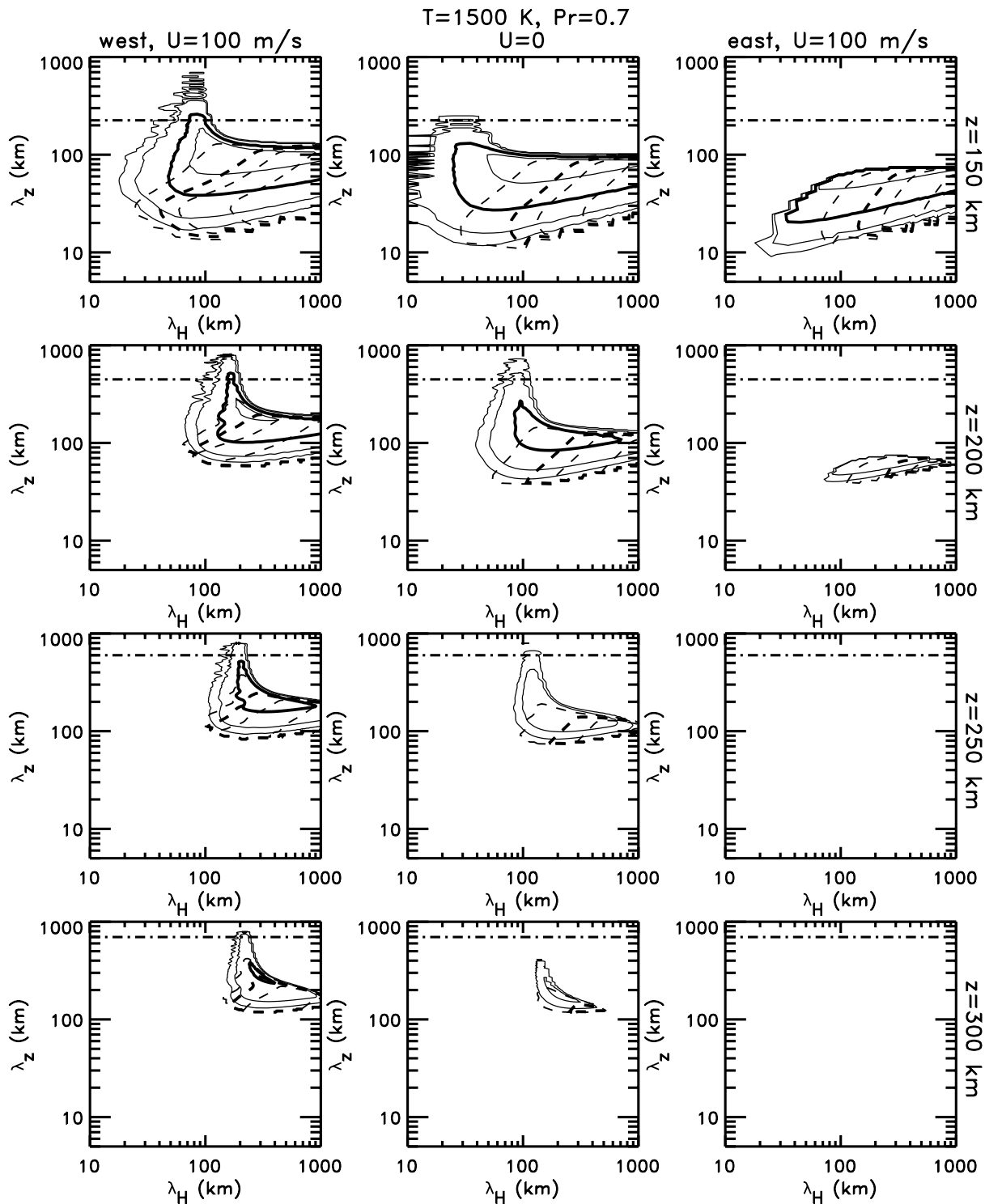
**Fig. 8.** As in Fig. 6, but for maximum solar forcing conditions ($\sim$1500 K thermospheric temperature).

to 0.5, and the ranges of $\lambda_h$ and $\lambda_z$ for which they occur at 250 km, increase substantially with higher thermospheric temperatures for the unshifted (meridionally propagating) GWs and up-shifted (westward-propagating) GWs. The major dif-

ferences at 250 km, compared to 200 km, are 1) decreases in the peak momentum flux fractions by $\sim$2 or less for the up-shifted GWs, 2) a somewhat larger momentum flux reduction for the unshifted GWs, and 3) a shift of both responses

to slightly larger $\lambda_h$ and $\lambda_z$. As suggested by the results in Figs. 3 and 4, this same trend also persists to 300 km (and above). Here we see comparable spatial scales, and further reduced, but still significant, surviving momentum flux fractions of $\sim 0.03$ to 0.5 and a bit less for the up-shifted and unshifted GWs, respectively, at maximum solar forcing, but with comparable responses at mean solar forcing only for the up-shifted GWs (see the lower left panels of Figs. 7 and 8). The important point here is that, depending on details of GW sources, refraction, and dispersion, the surviving GWs may achieve quite appreciable amplitudes, body forces, and influences relevant to a variety of neutral and plasma dynamics at these altitudes. Possible implications of these potentially large GWs are discussed further in the following section.

The spatial scales anticipated at 250 km for up-shifted and unshifted GWs (with westward and meridional propagation) are virtually the same for mean and maximum solar forcing (apart from small differences in surviving momentum flux fractions) in each case. They are also slightly larger than seen at 200 km, as noted above. In both cases, surviving momentum flux fractions of $\sim 0.5$ and above occur for up-shifted GWs at $\lambda_h \sim 170$ to 700 km and $\lambda_z \sim 150$ to 300 km. Comparable ranges for the largest remaining unshifted GWs at 250 km are only slightly smaller, $\lambda_h \sim 100$ to 400 km and $\lambda_z \sim 150$ to 250 km, but momentum flux fractions are smaller by $\sim 2$ to 5. Both surviving momentum flux fractions and the range of wavelengths are smaller again at 300 km, with only a tiny response for unshifted GWs at maximum solar forcing centered at $\lambda_h$ and $\lambda_z \sim 150$ to 300 km. Up-shifted responses at 300 km, in contrast, remain significant at maximum solar forcing, with fractional momentum fluxes of $\sim 0.1$ and larger occurring in the wavelength ranges $\lambda_h \sim 150$ to 1000 km and $\lambda_z \sim 150$ to 500 km, with an apparent maximum response again at $\lambda_h$ and $\lambda_z \sim 200$ to 300 km. The corresponding distribution of wavelengths is only slightly smaller at mean solar forcing, and appears centered at similar wavelengths. These spatial scales are largely consistent with those previously inferred from observations by Thome and Rao (1969) and Djuth et al. (1997, 2004) at Arecibo Observatory, by Oliver et al. (1997) at the MU radar, by Samson et al. (1990) with a SUPERDARN prototype at a higher latitude, and the predictions of V07. We note, however, that the larger vertical wavelengths now extend to, or beyond, the limits of applicability of WKB theory, suggesting caution in the quantitative application of these results at the largest vertical scales.

Referring to the dashed contours denoting observed periods in Figs. 6 to 8, we see that GWs having large surviving momentum flux fractions at 150 km have observed periods ranging from $\sim 10$ min to more than 1 h for all propagation directions and Doppler-shifting conditions. This is because dissipation is weak at this altitude for GWs at these spatial scales and mean winds have not yet achieved their highest magnitude. At 200 km, zonal winds are now near their maximum value, there is now a much larger disparity between

up-shifted and down-shifted GWs characteristics, and dissipation is significantly stronger. The result is that down-shifted and unshifted GWs propagating eastward or meridionally occur primarily at observed periods of $\sim 10$ to 30 min, whereas up-shifted GWs occur at periods from $\sim 10$ min to an hour or more (though the range of intrinsic periods is substantially shorter). At higher altitudes, the longer observed periods disappear first, with the surviving GWs having periods of $\sim 10$ min at 250 km under solar minimum forcing, and $\sim 10$ to 20 min and $\sim 10$ to 30 min, respectively, at 300 km under mean and maximum solar forcing. In each case then, the GWs surviving to the highest altitudes for any thermospheric temperature are increasingly confined to the highest frequencies and shortest periods for which vertical propagation remains possible.

Similar results, but for stronger Doppler shifting, are displayed in Fig. 9. Because down-shifted GWs fail to penetrate to higher altitudes, however, this figure shows only up-shifted GWs for the three thermospheric temperature profiles displayed in Fig. 1. Again, horizontal dashed lines in each panel indicate a vertical wavelength of $4\pi H$, near which the WKB approximation is expected to fail. Comparing these results with those shown in the left columns of Figs. 6 to 8, we see that stronger Doppler shifting typically enhances penetration altitudes (hence the surviving momentum flux fractions at any specific altitude) and increases the horizontal and vertical wavelengths occurring at any altitude. For every solar forcing condition, the maximum momentum flux fractions occurring at 300 km increase from $\sim 0.1$ to 0.5 for a mean wind of $100\,\mathrm{ms^{-1}}$ to $\sim 0.5$ to 0.9 for a mean wind of $100\,\mathrm{ms^{-1}}$. Corresponding horizontal and vertical wavelengths for each case also increase by $\sim 50\%$. Finally, we note that the intrinsic GW periods are essentially the same in each case, $\sim 10$ to 30 min, despite accompanying larger spatial scales for larger Doppler-shifting environments. Thus, up-shifting by stronger thermospheric winds pushes those GWs penetrating to the highest altitudes even closer to violation of the WKB condition for all solar forcing conditions.

## 5 Variations of GW momentum fluxes and body forces with altitude

To address the potential for GWs penetrating to high altitudes to impact neutral thermospheric and/or ionospheric processes, we now describe surviving momentum flux fractions and the relative body forces implied by each for the range of GW horizontal wavelengths and ground-based periods seen above to penetrate to the highest altitudes. We also do so for both up-shifted and down-shifted GWs to emphasize the importance of MLT and thermospheric winds in enhancing or suppressing components of the GW spectrum through refraction to larger or smaller vertical wavelengths (or Doppler shifting to higher or lower intrinsic phase speeds or frequencies). These results are shown in Figs. 10
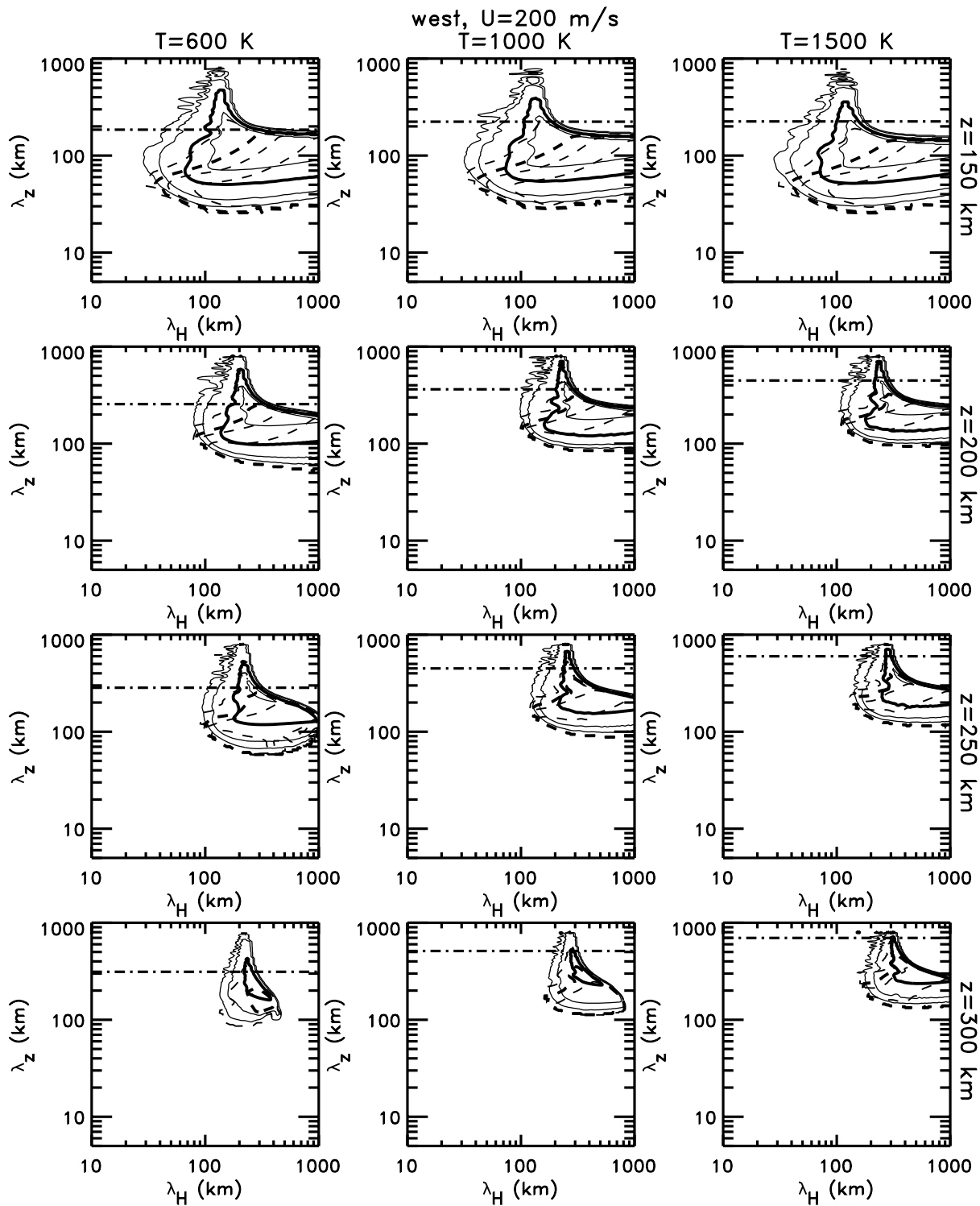
**Fig. 9.** As in Figs. 6 to 8, but for westward-propagating (up-shifted) GWs for minimum, mean, and maximum solar forcing (left, middle, and right columns, respectively) with an eastward thermospheric wind of $200 \, \mathrm{ms}^{-1}$.

and 11 for GWs having $\lambda_h$=100, 200, 300, and 400 km and ground-based periods of 15, 20, and 30 min for mean solar forcing (a thermospheric temperature of ~1000 K). Figures 10 and 11 are for eastward thermospheric winds of 100 and $200 \, \mathrm{ms}^{-1}$, respectively. Based on our results above, we expect these GWs to be most relevant to our exploration of
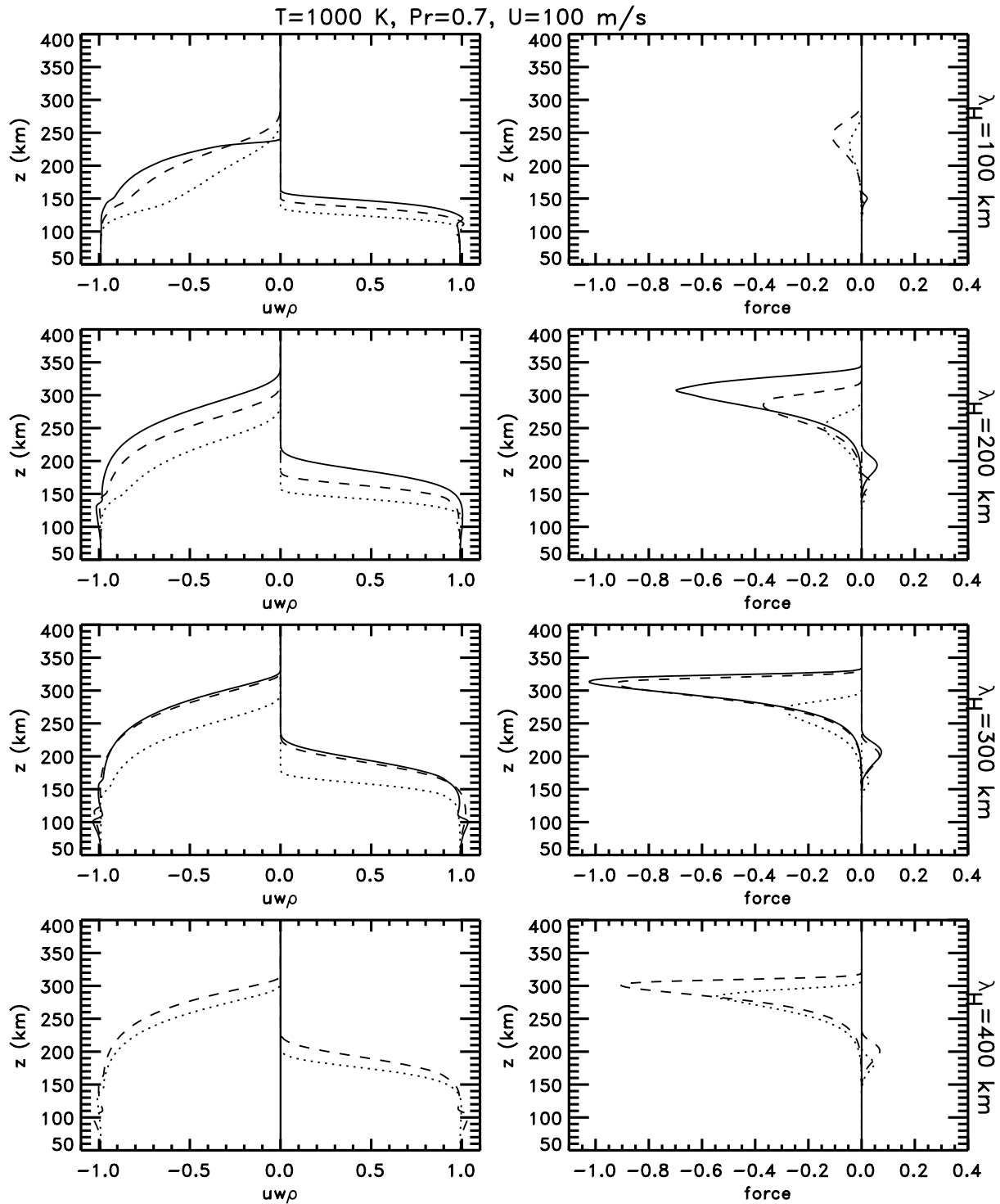
**Fig. 10.** Surviving momentum flux fractions (left panels) and normalized body forces (right panels) for up-shifted and down-shifted GWs (left and right sides of each panel), $\lambda_h$=100, 200, 300, and 400 km (top to bottom), mean solar forcing (a thermospheric temperature of $\sim$1000 K), and a thermospheric zonal wind of $100\,\mathrm{ms}^{-1}$. Ground-based periods are 15 (solid), 20 (dashed), and 30 min (dotted) in each case, except that $\lambda_h$=400 km is precluded by the $1/4H^2$ term in the bottom panels. Note that it is the up-shifted GWs of higher ground-based (and intrinsic) frequencies and intermediate $\lambda_h$ that penetrate to the highest altitudes and have the largest implied body forces. The exception is the 15-min period GW with $\lambda_h$=100 km, which is reflected at a turning level at an altitude of $\sim$240 km.
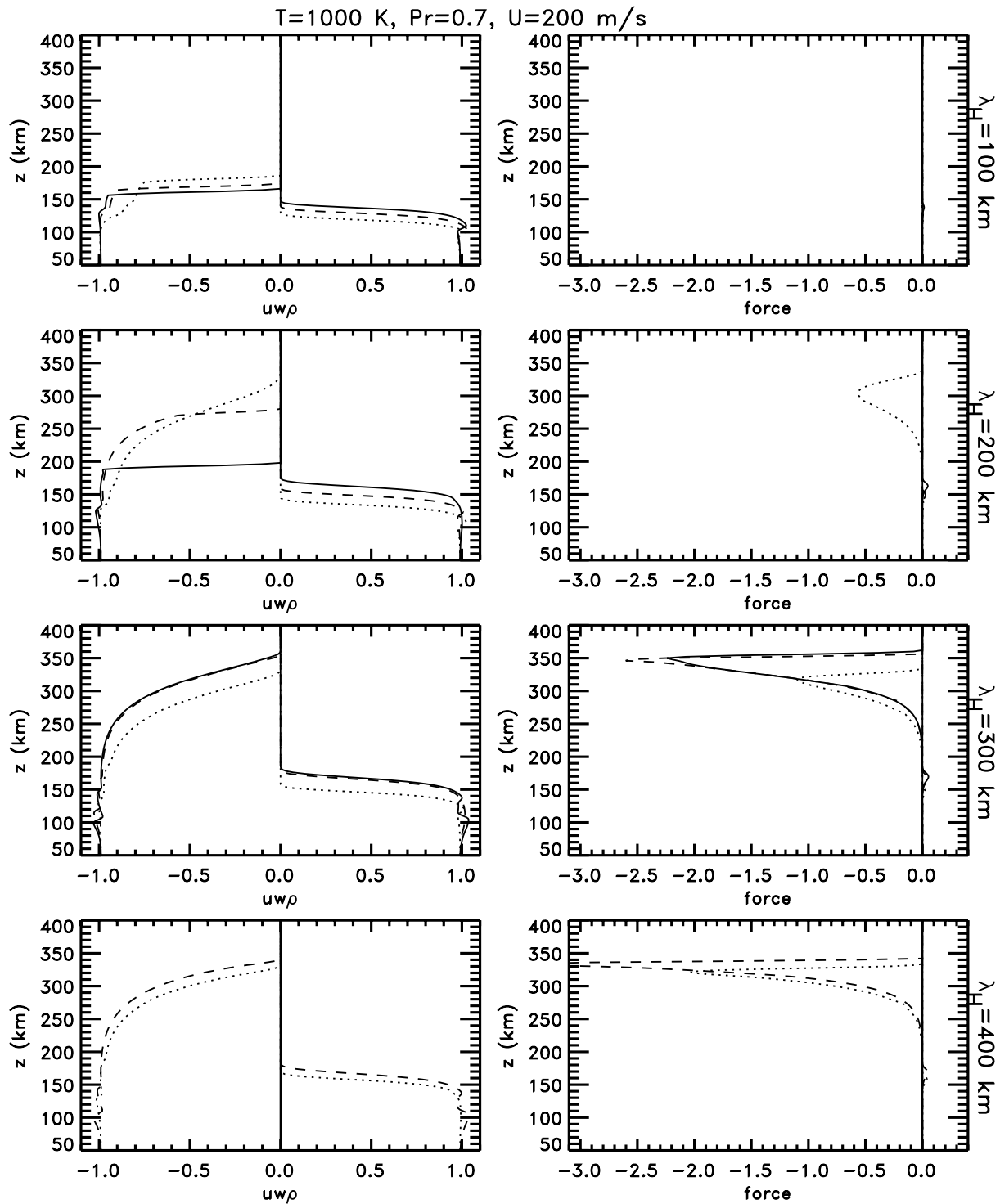
**Fig. 11.** As in Fig. 10, but for a thermospheric zonal wind of $200 \, \mathrm{ms}^{-1}$.

potential GW seeding of plasma instabilities, assuming these GWs arose from sources in the lower atmosphere.

Referring to Fig. 10, we see (consistent with our discussion above) that the up-shifted GWs for a thermospheric wind of $100 \, \mathrm{ms}^{-1}$ (experiencing increasing intrinsic phases speeds, frequencies, and vertical wavelengths) on the left

**Table 1.** Variations with altitude of mean density, $\rho_0(z)$, the areas over which momentum fluxes for a specific GW are distributed, $A(z)$, and the ratios of momentum flux and perturbation velocities for each GW, at thermospheric altitudes of 100, 150, 200, 250, and 300 km and a temperature of $\sim$1000 K. Values refer only to those GWs that attain the highest altitudes, and the momentum fluxes and velocities at 300 km vary somewhat due to differential dissipation among the various GWs that reach these altitudes.

| $z$ (km) | $\rho_0$ (g/m$^3$) | $A(z)/A$ (80 km) | $<u_h'w'>(z)/<u_h'w'>$ (80 km) | $u_h'$, $w'(z)/u_h'$, $w'$ (80 km) |
|---|---|---|---|---|
| 300 | $\sim 10^{-8}$ | $\sim$17 | $\sim 6\times 10^4$ (no dissipation) | $\leq$250 (with dissip.) |
| 250 | $\sim 7\times 10^{-8}$ | $\sim$12 | $\sim 10^4$ | $\sim$100 |
| 200 | $\sim 5\times 10^{-7}$ | $\sim$7 | $\sim 3\times 10^3$ | $\sim$50 |
| 150 | $\sim 5\times 10^{-6}$ | $\sim$4 | $\sim$500 | $\sim$20 |
| 100 | $\sim 10^{-3}$ | $\sim$1.6 | $\sim$6 | $\sim$2.5 |
| 80 | $\sim 10^{-2}$ | 1 | 1 | 1 |

side of each panel achieve systematically higher altitudes and larger body forces where they are dissipated than the down-shifted GWs (with decreasing intrinsic phases speeds, frequencies, and vertical wavelengths) on the right side of each panel. Also seen here in a different form than depicted in Figs. 2 to 5 are the rates of damping of the various GW motions. In particular, we see that up-shifted GWs decay more gradually with altitude than down-shifted GWs, due to a combination of their higher vertical group velocities and weaker dissipation at each altitude, both of which are due to their refraction to higher vertical wavelengths accompanying upstream propagation against increasing thermospheric winds. For both up-shifted and down-shifted GWs, it is also the highest frequencies (shortest ground-based and intrinsic periods) that experience initial dissipation at the highest altitudes, and again for the same reasons. The only exception is the up-shifted GW having $\lambda_h$=100 km and a period of 10 min. This GW experiences reflection at $\sim$240 km, with minimal dissipation prior to reflection.

Body forces accompanying the dissipation of those GWs that avoid reflection are displayed in the right panels of Fig. 10. In all cases they are normalized relative to the largest body force (occurring for the GW with $\lambda_h$=300 km and a period of 15 min). Three different horizontal wavelengths contribute potentially strong body forces peaking above 300 km ($\lambda_h$=200, 300, and 400 km), with 15-min periods doing so at the shorter two wavelengths and 20-min periods doing so at the longer two wavelengths. The other GWs displayed also contribute large relative body forces at somewhat lower altitudes, and all have the potential to induce significant perturbations at bottomside F layer altitudes if they are excited with sufficient amplitudes. GWs having large surviving momentum fluxes and associated body forces at high altitudes contribute two potential influences of GWs on plasma instability processes. One is the direct influence of GW perturbations on neutral and/or plasma quantities, gradients, drifts, fields, conductivities, etc. The second is the indirect influence on neutral and/or plasma quantities of induced mean motions (and gradients) accompanying GW dissipation. The

latter, in particular, may contribute to neutral winds, horizontal plasma drifts, and their vertical gradients and differences. Indeed, it could prove to be a combination of GW perturbations and induced "mean" effects that has the greatest cumulative impact on plasma instability growth rates and plasma bubble initiation. The relative magnitudes of these competing contributions to plasma and neutral perturbations at bottomside F layer altitudes are addressed in greater detail by Fritts et al. (2008c) and Abdu et al. (2008) in this issue. These authors assess, respectively, 1) the magnitudes of GW perturbations at bottomside F layer altitudes based on SpreadFEx observations and theory and 2) the impacts of these GW perturbations on various instability growth rates for various GW scales, frequencies, amplitudes, and propagation directions. Here, we try only to estimate the relative increases of GW amplitude and momentum flux compared to magnitudes observed in the MLT.

From 80 km to $\sim$300 km, at which we estimate the dominant up-shifted GWs arising in the lower atmosphere to dissipate (under mean solar forcing conditions and with a thermospheric wind of 100 ms$^{-1}$), mean density decreases by $\sim 10^6$ (Fig. 1) but momentum fluxes decrease by only $\sim$4 (Fig. 10), excluding dispersion effects. Dispersion implies further reductions in mean momentum flux for any GW, and we assume this reduction is proportional to $1/r^2$ from sources in the troposphere, which we assume for simplicity to be $\sim$10 km. For conservative GW propagation, we have the following relation,

$$\rho_0(z) < u_h'w' > (z)A(z) = \rho_0(80) < u_h'w' > (80)A(80)$$
$$= \rho_0(0) < u_h'w' > (0)A(0) \quad (4)$$

where $\rho_0(z)$ is mean density at altitude $z$, $\rho_0(z)<u_h'w'>(z)$ is the GW momentum flux at altitude $z$, brackets denote an average over GW phase, and $A(z)$ is the relative area over which the momentum flux occurs at altitude $z$. We can then easily estimate the relative momentum fluxes and velocity perturbations at thermospheric altitudes relative to those at the mesopause. The various quantities are listed for altitudes of 80, 100, 150, 200, 250, and 300 km in Table 1 for

easy reference. Note that while there are orders of magnitude variations in mean density from the lowest to the highest altitudes, variations in momentum flux and GW perturbation velocities are relatively much smaller over thermospheric altitudes of ∼200 to 300 km. This occurs because 1) there are fewer scale heights from 200 to 300 km than from 80 to 200 km, 2) dispersion continues to occur in the thermosphere, and 3) dissipation of even these GWs having the largest scales and frequencies is significant by ∼300 km. These are nevertheless very large amplification factors, and they suggest that if these large-scale and high-frequency GWs are efficiently excited by deep convection, even at very small amplitudes and momentum fluxes in the lower atmosphere and MLT, they may achieve large amplitudes and fluxes and make important contributions to neutral and/or plasma dynamics in the thermosphere. For example, a GW contributing horizontal and vertical velocity perturbations of ∼100 ms$^{-1}$ at ∼250 km (and having a momentum flux at these altitudes of ∼$10^4$ m$^2$ s$^{-2}$), and thus potentially contributing significantly to plasma instability processes, would have amplitudes and a momentum flux at 80 km of ∼1 ms$^{-1}$ and ∼0.5 m$^2$ s$^{-2}$, respectively. But these would be entirely undetectable relative to larger contributions at smaller GW scales and frequencies often seen at 80 km (Table 1; Fritts and Alexander, 2003; Vargas et al., 2008).

Results corresponding to those shown in Fig. 10 for selected up-shifted and down-shifted GWs, but for a thermospheric wind of 200 ms$^{-1}$, are displayed in Fig. 11. In this case, a larger fraction of the up-shifted GWs at shorter periods and horizontal wavelengths encounter turning levels, causing the high-altitude responses to shift to longer periods and scales. In this case, all up-shifted GWs having $\lambda_h$=100 km are reflected between ∼160 and 190 km, while the two shorter-period GWs having $\lambda_h$=200 km are reflected at ∼200 and 280 km, respectively. Down-shifted GWs for the stronger thermospheric winds also are dissipated at lower altitudes, as discussed above. However, the up-shifted GWs that do not encounter turning levels are seen to penetrate to higher altitudes than under weaker Doppler-shifting conditions. As a result, these GWs also attain larger amplitudes and momentum fluxes at the highest altitudes. The body forces shown in Fig. 11 are scaled by the same factor employed in Fig. 10 to show the relative effects (note the different scale for body force magnitudes). The effect is penetration to only slightly higher altitudes (by ∼30 km) and with slightly larger amplitudes (by ∼2 times), with these occurring only at the highest altitudes seen in Fig. 1 and displayed in Table 1.

Finally, we note that our analysis here has focused entirely on GWs arising from sources in the lower atmosphere, for which there are WKB constraints on the initial vertical wavelengths (or horizontal phase speeds), and corresponding horizontal wavelengths, that can reach very high altitudes (Eq. 3; V07). These constraints are less severe for GWs arising at higher altitudes, however, because of the increasing

temperatures and scale heights in the thermosphere. Thus we expect that primary sources at much higher altitudes, such as auroral excitation (Hocke and Schlegel, 1996, and references cited above), and secondary sources such as local body forces (Vadas and Fritts, 2001, 2002) must also excite GWs at substantially larger spatial scales that can penetrate, in turn, to even higher altitudes, as observed by various authors (Oliver et al., 1997; Djuth et al., 1997, 2004; Livneh et al., 2007). We expect these GWs to have very small initial amplitudes and momentum fluxes, as for the larger scales excited by lower atmosphere sources, but to also experience dramatic amplification factors in propagating to altitudes of 300 km and above. Such GWs would also be refracted by MLT and thermospheric winds, but to a smaller degree than the smaller-scale GWs arising at lower altitudes and having smaller intrinsic phase speeds. Thus, GWs having larger spatial scales and arising from sources higher in the atmosphere will also be more isotropic in their direction of propagation, and in particular, will experience propagation to high altitudes and significant amplification for a greater range of Doppler-shifting conditions. And given their apparent ubiquitous presence at high altitudes, we should expect that they will also contribute to any perturbation fields that might participate in seeding plasma instabilities at the bottomside F layer.

## 6 Summary and conclusions

We have focused in this paper on how refraction due to Doppler shifting and variable thermospheric temperatures, and dissipation due to kinematic viscosity and thermal diffusivity, influence the horizontal and vertical wavelengths and observed periods of GWs arising from sources in the lower atmosphere and penetrating to the highest altitudes in the thermosphere. WKB theory limits the horizontal and vertical wavelengths that can be ray traced with confidence, thus also restricting the range of wavelengths (for GWs propagating vertically) that can readily be attributed to lower atmospheric sources. This does not restrict the spatial scales that can occur in the thermosphere, nor does it mean that larger scales cannot arise in the lower atmosphere. But it suggests that GWs having larger vertical scales because of very high horizontal phase speeds (∼250 ms$^{-1}$ or larger) before strong up-shifting in the thermosphere more likely arise from sources, such as auroral energy deposition or body forces due to local GW dissipation, at considerably higher altitudes.

For those GWs that can be ray traced from the lower atmosphere, we found three primary influences on GW survival and penetration to high altitudes, all of which have major impacts on some portion of the GW spectrum. Refraction accompanying Doppler shifting by strong mean winds in the MLT and thermosphere was found to strongly favor penetration to high altitudes by GWs that are up-shifted to

higher intrinsic frequencies and vertical wavelengths, rather than down-shifted to lower intrinsic frequencies and vertical wavelengths. The differences in penetration altitudes between up-shifted and down-shifted components for a thermospheric wind of $100\,\mathrm{ms}^{-1}$ vary from $\sim$50 km for minimum solar forcing and thermospheric temperatures to over 100 km for maximum solar forcing and thermospheric temperatures. Differences are even larger, $\sim$150 to 200 km, for a thermospheric wind of $200\,\mathrm{ms}^{-1}$ and mean solar forcing and thermospheric temperatures.

A second factor that plays a large role in limiting vertical propagation, but only for up-shifted GWs, is GW evanescence and reflection at turning levels that occurs both due to increasing intrinsic phase speeds (and intrinsic frequencies) and decreasing thermospheric stability. Reflection prevents vertical propagation for the majority of the horizontal wavelengths at the observed frequency of $\omega_r$=N/2, and for an intermediate range of horizontal wavelengths for $\omega_r$=N/3, for all solar conditions, thermospheric temperatures, and a thermospheric wind of $100\,\mathrm{ms}^{-1}$ (see Figs. 2 to 4). For maximum solar forcing, only the highest allowed horizontal wavelengths survive for $\omega_r$=N/2, with an expanded range of large horizontal wavelengths penetrating to even higher altitudes for lower observed frequencies. Similar tendencies occur under minimum solar forcing, but without the preferential penetration for lower observed frequencies, and responses for mean solar conditions are between these two extremes.

These tendencies are accentuated further for a thermospheric wind of $200\,\mathrm{ms}^{-1}$, where up-shifted GWs with $\omega_r$=N/2 at essentially all horizontal wavelengths encounter turning levels under all solar forcing conditions. Increasing fractions of the larger horizontal wavelengths penetrate to higher altitudes as initial frequencies decrease, though this is restricted to only the largest horizontal wavelengths for $\omega_r$=N/3. GWs also penetrate to higher altitudes at each frequency as thermospheric temperatures increase. The net result is penetration to the highest altitudes for strongly up-shifted GWs at $\omega_r\sim$N/3 to N/5 under mean solar forcing conditions, but preferred penetration to the highest altitude at $\omega_r\sim$N/5 to N/10 under maximum solar forcing conditions at even larger horizontal wavelengths.

The final factor impacting GW penetration altitudes is viscous dissipation that acts most strongly on GWs having smaller spatial scales and lower intrinsic frequencies. This accounts for the differences in penetration altitudes among those GWs surviving reflection. It also causes a concentration of surviving GWs at $\lambda_h\sim$150 to 1000 km (with the larger values for stronger solar forcing) and $\lambda_z\sim$100 to 500 km (again with the larger values for stronger solar forcing testing the limits of WKB theory) and the highest allowed intrinsic frequencies (but longer observed GW periods of $\sim$10 to 30 min) for moderate Doppler shifting ($\sim$100 ms$^{-1}$), with the surviving spatial scales and observed periods increasing further under stronger Doppler-shifting conditions. Note again that these larger inferred vertical wavelengths are ex-

tending to (and beyond) those for which WKB theory is applicable.

We also assessed GW amplitude and momentum flux variations in the thermosphere as amplification factors relative to their values at 80 km. Because the most rapid density decreases with altitude occur at lower altitudes, GWs arising from local sources in the lower atmosphere experience dispersion with increasing altitude, and dissipation plays the dominant role at the highest altitudes, amplitude amplification factors relative to 80 km vary in an apparently restricted range of $\sim$40 to 150 at altitudes from $\sim$200 to 300 km. These amplification factors are nevertheless sufficiently large to allow GWs having undetectable amplitudes and momentum fluxes in the MLT to potentially make major perturbations to neutral and/or plasma quantities, gradients, drifts, fields, and conductivities, etc., and to plasma instability growth rates, at the bottomside F layer for all solar forcing conditions and thermospheric temperatures. We also anticipate that the body forces accompanying GW transience and dissipation may themselves lead to large perturbations in mean winds, plasma drifts, and gradients that may also contribute to instability growth rates. Finally, we noted that there are GWs that penetrate to even higher altitudes in the thermosphere than cannot be explained due to lower atmospheric sources and ray tracing. These GWs must arise at higher altitudes, may have larger spatial scales allowing higher penetration altitudes, and may likewise experience significant amplitude amplification through vertical propagation. As such, they may contribute additional perturbations, and potentially with other orientations and phase relations, to the geophysical variability potentially influencing plasma instability processes at the bottomside F layer.

## References

Abdu, M., Kherani, E., Batista, I., et al.: Gravity wave influences on plasma instability growth rates based on observations during the Spread F Experiment (SpreadFEx), Ann. Geophys., in review, 2008.

Alexander, M. J., Holton, J. R., and Durran, D. R.: The gravity wave response above deep convection in a squall line simulation, J. Atmos. Sci., 52, 2212–2226, 1995.

Anderson, D. N., Richmond, A. D., Balsley, B. B., Roble, R. G., Biondi, M. A., and Sipler, D. P.: In situ generation of gravity waves as a possible seeding mechanism for equatorial spread-F, Geophys. Res. Lett., 9, 789–792, 1982.

Bauer, S. J.: An apparent ionospheric response to the passage of hurricanes, J. Geophys. Res., 63, 265–269, 1958.

Bishop, R., Aponte, N., Earle, G. D., Sulzer, M., Larsen, M. F., and Peng, G.: Arecibo observations of ionospheric perturbations

associated with the passage of tropical storm Odette, J. Geophys. Res., 111, A11320, doi:10.1029/2006JA011668, 2006.

Crowley, G., Jones, T. B., and Dudeney, J. R.: Comparison of short period TID morphologies in Antarctica during geomagnetically quiet and active intervals, J. Atmos. Terres. Phys., 49, 1155–1162, 1987.

Dewan, E. M., Picard, R. H., O'Neil, R. R., Gardiner, H. A., Gibson, J., Mill, J. D., Richards, E., Kendra, M., and Gallery, W. O.: MSX satellite observations of thunderstorm-generated gravity waves in mid-wave infrared images of the upper stratosphere, Geophys. Res. Lett., 25, 939–942, 1998.

Djuth, F. T., Sulzer, M. P., Elder, J. H., and Wickwar, V. B.: High-resolution studies of atmosphere-ionosphere coupling at Arecibo Observatory, Puerto Rico, Radio Sci., 32, 2321–2344, 1997.

Djuth, F. T., Sulzer, M. P., Gonzales, S. A., Mathews, J. D., Elder, J. H., and Walterscheid, R. L.: A continuum of gravity waves in the Arecibo thermosphere?, Geophys. Res. Lett., 31, L16801, doi:10.1029/2003GL019376, 2004.

Francis, S. H.: Acoustic-gravity modes and large-scale traveling ionospheric disturbances of a realistic, dissipative atmosphere, J. Geophys. Res., 78, 2278–2301, 1973.

Fritts, D. C., Abdu, M. A., Batista, B. R., et al.: Overview and Summary of the Spread F Experiment (SpreadFEx), Ann. Geophys., in press, 2008a.

Fritts, D. C., Abdu, M. A., Batista, B. R., et al.: The Spread F Experiment (SpreadFEx): Program overview and first results, Earth, Planets and Space, CPEA special issue, in press, 2008b.

Fritts, D. C., Vadas, S. L., Riggin, D. M., et al.: Gravity wave influences on equatorial spread F based on observations during the Spread F Experiment (SpreadFEx), Ann. Geophys., 26, 3235–3252, 2008c,
http://www.ann-geophys.net/26/3235/2008/.

Fritts, D. C. and Alexander, M. J.: Gravity dynamics and effects in the middle atmosphere, Rev. Geophys., 41(1), 1003, doi:10.1029/2001RG000106, 2003.

Fritts, D. C., Vadas, S. L., Wan, K., and Werne, J. A.: Mean and variable forcing of the middle atmosphere by gravity waves, J. Atmos. Solar-Terr. Phys., 68, 247–265, 2006.

Fritts, D. C., Vadas, S. A., and Yamada, Y.: An estimate of strong local gravity wave body forcing based on OH airglow and meteor radar observations, Geophys. Res. Lett., 29(10), 1429, doi:10.1029/2001GL013753, 2002.

Georges, T. M.: HF Doppler studies of traveling ionospheric disturbances, J. Atmos. Terr. Phys., 30, 735–746, 1968.

Hearn, A. L. and Yeh, K. C.: Medium scale TIDs and their associated internal gravity waves as seen through height-dependent electron density power spectra, J. Geophys. Res., 82, 4983–4990, 1977.

Hickey, M. P. and Cole, K. D.: A quartic dispersion relation for internal gravity waves in the thermosphere, J. Atmos. Terres. Phys., 49, 889–899, 1987.

Hickey, M. P. and Cole, K. D.: A numerical model for gravity wave dissipation in the thermosphere, J. Atmos. Terres. Phys., 50, 689–697, 1988.

Hines, C. O.: Internal atmospheric gravity waves at ionospheric heights, Can. J. Phys., 38, 1441–1481, 1960.

Hines, C. O.: On the nature of traveling ionospheric disturbances launched by low-altitude nuclear explosions, J. Geophys. Res., 72, 1877–1882, 1967.

Hocke, K. and Schlegel, K.: A review of atmospheric gravity waves and traveling ionospheric disturbances: 1982–1995, Ann. Geophys., 14, 917–940, 1996,
http://www.ann-geophys.net/14/917/1996/.

Hocke, K., Schlegel, K., and Kirchengast, G.: Phases and amplitudes of TIDs in the high-latitude F-region observed by EISCAT, J. Atmos. Terres. Phys., 58, 245–255, 1996.

Hocke, K. and Tsuda, T.: Gravity waves and ionospheric irregularities over tropical convection zones observed by GPS/MET radio occultation, Geophys. Res. Lett., 28, 2815–2818, 2001.

Horinouchi, T., Nakamura, T., and Kosaka, J.: Convectively generated mesoscale gravity waves simulated throughout the middle atmosphere, Geophys. Res. Lett., 29(21), 2007, doi:10.1029/2002GL016069, 2002.

Hung, R. J. and Kuo, J. P.: Ionospheric observation of gravity-waves associated with hurricane Eloise, J. Geophys. Res., 45, 67–80, 1978.

Hung, T. P., and Smith, R. E.: Observations of gravity waves during the extreme tornado outbreak of 3 April 1974, J. Atmos. Terres. Phys., 40, 831–843, 1978.

Hung, R. J. and Smith, R. E.: Ray tracing of gravity waves as a possible warning system for tornadic storms and hurricanes, J. Appl. Meteor., 17, 3–11, 1978.

Lane, T. P. and Clark, T. L.: Gravity waves generated by the dry convective boundary layer: two-dimensional scale selection and boundary layer feedback, Q. J. Roy. Meteorol. Soc., 128, 1543–1570, 2002.

Lane, T. P., Reeder, M. J., and Clark, T. L.: Numerical modeling of gravity waves generated by deep tropical convection, J. Atmos. Sci., 58, 1249–1274, 2001.

Livneh, D. J., Seker, I., Djuth, F. T., and Mathews, J. D.: Continuous quasiperiodic thermospheric waves over Arecibo, J. Geophys. Res., 112, A07313, doi:10.1029/2006JA012225, 2007.

Marks, C. J. and Eckermann, S. D.: A three-dimensional nonhydrostatic ray-tracing model for gravity waves: formulation and preliminary results for the middle atmosphere, J. Atmos. Sci., 52, 1959–1984, 1995.

McClure, J. P., Singh, S., Bamgboye, D. K., Johnson, F. S., and Kil, H.: Occurrence of equatorial F region irregularities: Evidence for tropospheric seeding, J. Geophys. Res., 103, 29 119–29 135, 1998.

Ogawa, T., Igarashi, K., Aikyo, K., and Maeno, H.: NNSS satellite observations of medium-scale traveling ionospheric disturbances at southern high-latitudes, J. Geomag. Geoelectr., 39, 709–721, 1987.

Oliver, W. L., Otsuka, Y., Sato, M., Takami, T., and Fukao, S.: A climatology of F region gravity wave propagation over the middle and upper atmosphere radar, J. Geophys. Res., 102, 14 499–14 512, 1997.

Piani, C., Durran, D., Alexander, M. J., and Holton, J. R.: A numerical study of three-dimensional gravity waves triggered by deep tropical convection, J. Atmos. Sci., 57, 3689–3702, 2000.

Pitteway, M. L. V. and Hines, C. O.: The viscous damping of atmospheric gravity waves, Can. J. Phys., 41, 1935–1948, 1963.

Richmond, A. D.: Gravity wave generation, propagation, and dissipation in the thermosphere, J. Geophys. Res., 83, 4131–4145, 1978.

Röttger, J.: Atmospheric gravity waves generated by penetrative cumulus convection in the tropics, 11th Conference on Hurri-

canes and Tropical Meteorology, AMS, Florida, 13–16 December 1977.

Samson, J. C., Greewald, R. A., Ruohonniemi, J. M., Frey, A., and Baker, K. B.: Goose Bay radar observations of Earth-reflected atmospheric gravity waves in the high-latitude ionosphere, J. Geophys. Res., 95, 7693–7709, 1990.

Sentman, D. D., Wescott, E. M., Picard, R. H., Winick, J. R., Stenbaek-Nielson, H. C., Dewan, E. M., Moudry, D. R., São Sabbas, F. T., and Heavner, M. J.: Simultaneous observation of mesospheric gravity waves and sprites generated by a Midwestern thunderstorm, J. Atmos. Solar-Terres. Phys., 65, 537–550, 2003.

Taylor, M. J. and Hapgood, M. A.: Identification of a thunderstorm as a source of short period gravity waves in the upper atmospheric nightglow emissions, Planet. Space Sci., 36, 975–985, 1988.

Thome, G. D. and Rao, P. B.: Comparison of acoustic-gravity wave theory with UHF observations, Final Report, 62 pp., Raytheon Corp., Spencer Lab., Burlington, MA, May 1969.

Tsuda, T., Nishida, M., and Rocken, C.: A global morphology of gravity wave activity in the stratosphere revealed by the GPS occultation data (GPS/MET), J. Geophys. Res., 105, 7257–7274, 2000.

Vadas, S. L.: Horizontal and vertical propagation, and dissipation of gravity waves in the thermosphere from lower atmospheric and thermospheric sources, J. Geophys. Res., 112, A06305, doi:10.1029/2006JA011845, 2007.

Vadas, S. L. and Fritts, D. C.: Gravity wave radiation and mean responses to local body forces in the atmosphere, J. Atmos. Sci., 58, 2249–2279, 2001.

Vadas, S. L. and Fritts, D. C.: The importance of spatial variability in the generation of secondary gravity waves from local body forces, Geophys. Res. Lett., 29(20), 1984, doi:10.1029/2002GL015574, 2002.

Vadas, S. L. and Fritts, D. C.: Thermospheric responses to gravity waves arising from mesoscale convective complexes, J. Atmos. Solar Terres. Phys., 66, 781–804, 2004.

Vadas, S. L. and Fritts, D. C.: Thermospheric responses to gravity waves: Influences of increasing viscosity and thermal diffusivity, J. Geophys. Res., 110, D15103, doi:10.1029/2004JD005574, 2005.

Vadas, S. L. and Fritts, D. C.: The influence of increasing temperature and solar variability on gravity wave structure and dissipation in the thermosphere, J. Geophys. Res., TIMED special issue, 111, A10812, doi:10.1029/2005JA011510, 2006.

Vadas, S. L., Fritts, D. C., and Alexander, M. J.: Mechanism for the generation of secondary waves in wave breaking regions, J. Atmos. Sci., 60, 194–214, 2003.

Waldock, J. A. and Jones, T. B.: HF Doppler observations of traveling ionospheric disturbances at mid-latitudes, J. Atmos. Terres. Phys., 48, 245–260, 1986.

Waldock, J. A. and Jones, T. B.: Source regions of medium scale traveling ionospheric disturbances observed at mid-latitudes, J. Atmos. Terres. Phys., 49, 105–114, 1987.

Yeh, K. C., Liu, C. H., and Youakim, M. Y.: Attenuation of internal gravity waves in model atmospheres, Ann. Geophys., 31, 321–328, 1975,
http://www.ann-geophys.net/31/321/1975/.